Journal of Pharmaceutical Innovation (2026) 21:395
https://doi.org/10.1007/s12247-026-10636-5

RESEARCH

Preliminary Insight into the Antifungal and Anti-melanogenic Potential of a Xanthenone-based Hit Compound: In Vitro and In Vivo Zebrafish Evaluation

Amirah Hani Ramli[1] · Puspanjali Swain[2] · E. H. T. Thulshan Jayathilaka[3] · Mawalle Kankanamge Hasitha Madhawa Dias[3] · Muhammad Syafiq Akmal Mohd Fahmi[1] · Emilia Abdul Malek[4] · Yaya Rukayadi[1,5] · Kok Wai Lam[6] · Yee Seng Tan[7] · Chien Ing Yeo[7] · Cheol-Hee Kim[2] · Mahanama De Zoysa[3] · Siti Munirah Mohd Faudzi[1,4]

Received: 31 December 2025 / Accepted: 21 March 2026

Abstract

Purpose The emergence of multidrug-resistant *Candida auris* highlights the urgent need for alternative antifungal agents. This study evaluates the biological potential of xanthenones (**XA1**, **XA2**, **XA3**), previously synthesized xanthone derivatives with unexplored bioactivity, focusing on their antifungal efficacy and anti-melanogenic activity.

Methods All hydroxathenones were first screened in vitro against a series of pathogens. The active compound was then comprehensively tested against *C. auris*, with minimum inhibitory concentration (MIC) testing and mechanistic assays conducted to assess membrane permeability disruption, reactive oxygen species (ROS) production, and biofilm inhibition. Cytotoxicity was examined in HaCaT keratinocytes and B16F10 melanoma cells. Anti-melanogenic activity was assessed through in vitro tyrosinase inhibition and melanin quantification, followed by in vivo pigmentation analysis in zebrafish embryos, with kojic acid as a reference standard.

Results The most active analogue, 7-hydroxy-2,3,4,4,4a-tetrahydro-1*H*-xanthen-1-one (**XA3**), exhibited an MIC of 100 µg/mL against *C. auris*. Mechanistic investigations indicated disruption of fungal cell integrity through increased membrane permeability and elevated ROS production, contributing to reduced biofilm formation. Cytotoxicity assays showed acceptable safety profiles, with HaCaT keratinocytes retaining 85% viability at 25 µg/mL and consistent tolerance observed in B16F10 melanoma cells. Additionally, **XA3** demonstrated potent anti-melanogenic activity, significantly reducing tyrosinase activity, melanin content, and zebrafish embryo pigmentation, comparable to kojic acid.

Amirah Hani Ramli and Puspanjali Swain contributed equally to this work.

✉ Cheol-Hee Kim
zebrakim@cnu.ac.kr

✉ Mahanama De Zoysa
mahanama@cnu.ac.kr

✉ Siti Munirah Mohd Faudzi
sitimunirah@upm.edu.my

[1] Natural Medicines and Product Research Laboratory, Institute of Bioscience, Universiti Putra Malaysia, Serdang 43400, Selangor, Malaysia

[2] Department of Biology, Chungnam National University, Daejeon 34134, Republic of Korea

[3] College of Veterinary Medicine and Research Institute of Veterinary Medicine, Chungnam National University, Daejeon 34134, Republic of Korea

[4] Department of Chemistry, Faculty of Science, Universiti Putra Malaysia, Serdang 43400 UPM, Selangor, Malaysia

[5] Department of Food Science, Faculty of Food Science and Technology, Universiti Putra Malaysia, Serdang 43400 UPM, Selangor, Malaysia

[6] Drug and Herbal Research Centre Faculty of Pharmacy, Universiti Kebangsaan Malaysia, Jalan Raja Muda Abd. Aziz, Kuala Lumpur 50300, Malaysia

[7] Sunway Biofunctional Molecules Discovery Centre, School of Medical and Life Sciences, Sunway University, 47500 Bandar Sunway, , Petaling Jaya, Selangor Darul Ehsan, Malaysia

Conclusion This study presents the first preliminary report of the biological activity of **XA3**, highlighting its antifungal and anti-melanogenic effects at distinct concentration ranges. These findings position **XA3** as an early-stage hit compound with separate pharmacological properties that require further investigation.

Graphical Abstract

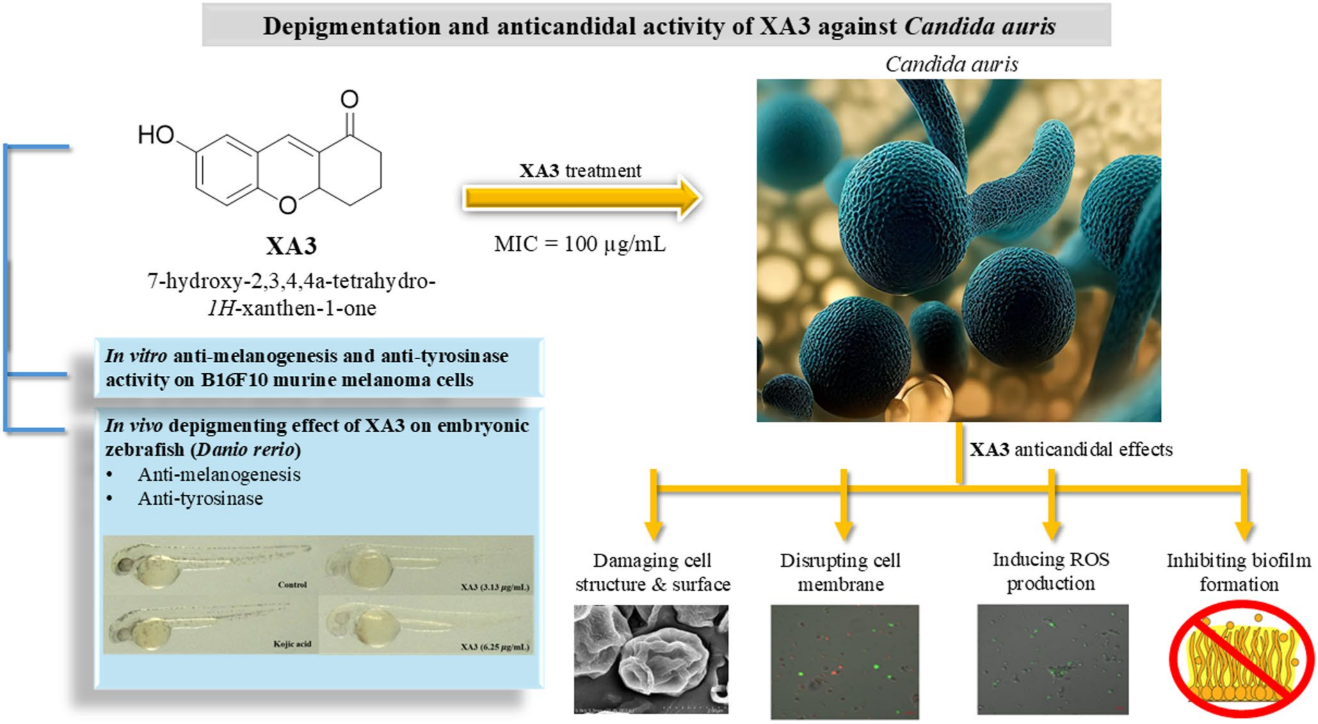

Keywords *Candida auris* · Antifungal · Biofilm inhibition · Anti-melanogenic · Hydroxyxanthenone · Zebrafish model

Introduction

Candida auris is a multidrug-resistant fungal pathogen of global concern, spreading rapidly in over 30 countries and associated with a high mortality rate, particularly among immunocompromised patients [1]. Its persistence on medical device surfaces and resistance to standard antifungal agents such as fluconazole and echinocandins significantly limit treatment options and complicate infection control [2–4]. Agents such as tigecycline and atovaquone impair mitochondrial function and energy production, leading to fungal cell death [5]. However, the efficacy of these drugs is compromised by the strong biofilm-forming ability of C. auris. These biofilms, composed of structured microbial communities within a protective extracellular matrix, are highly resistant to antifungal agents and evade the immune response [6]. Therefore, there is an urgent need for new drug candidates capable of penetrating and destroying these biofilms to improve treatment outcomes [7, 8].

In response to this therapeutic challenge, researchers are investigating alternative drug candidates, including xanthones and their xanthenone derivatives (Fig. 1). These compounds exhibit a broad range of pharmacological properties, including potent antifungal and antimicrobial activities via various mechanisms of action [9–13]. Hydroxyxanthones have attracted considerable interest because the hydroxyl groups enhance free radical scavenging, improve bioavailability, and facilitate interaction with fungal membranes [14–18]. Specific substitution patterns, such as 1,3-dihydroxylation, are associated with greater biofilm penetration and antifungal efficacy [19, 20], as well as to low cytotoxicity to mammalian cells [21, 22].

Interestingly, some fungal skin infections can be followed by post-inflammatory hyperpigmentation, which may complicate treatment and cosmetic outcomes [23, 24]. Although antifungal therapy resolves the underlying infection, pigmentary alterations may persist and often require independent dermatological intervention. Melanogenesis, the process of melanin production, is primarily regulated by tyrosinase, a copper-dependent enzyme that catalyzes key steps in melanin biosynthesis. Excess melanin production can cause hyperpigmentation disorders such as melasma, freckles, and age spots, increasing interest in alternative anti-melanogenic agents [25]. Several xanthones have demonstrated stronger tyrosinase inhibition than the reference standard kojic acid [26]. Molecular docking studies suggest that these compounds act via allosteric inhibition of tyrosinase, providing greater specificity and fewer side effects than conventional inhibitors [26]. Additionally, structure–activity relationship (SAR) analyses show that hydroxyl and methoxy groups enhance both tyrosinase inhibition and antioxidant activity, supporting their potential as effective anti-melanogenic agents. Together, these findings indicate that hydroxanthone derivatives may exhibit antifungal and anti-melanogenic properties through different underlying mechanisms.

In this study, three xanthenones, 2,3,4,4a-tetrahydro-1*H*-xanthen-1-one (**XA1**), 7-methoxy-2,3,4,4a-tetrahydro-1*H*-xanthen-1-one (**XA2**) and 7-hydroxy-2,3,4,4a-tetrahydro-1*H*-xanthen-1-one (**XA3**), as depicted in Fig. 1, were synthesized and characterized using spectroscopic and molecular structural analyses. Their comprehensive antifungal activities against *C. auris*, as well as the in vitro and in vivo anti-melanogenic potential of the most active derivative, were evaluated using B16F10 melanoma cells and zebrafish models. By exploring the structural versatility and bioactivities of hydroxyxanthones, this research aims to support the development of compounds that may be independently optimized for antifungal or anti-melanogenic applications.

Results and Discussion

Synthesis and Molecular Characterization of Xanthenones

The xanthenone derivatives, **XA1**, **XA2** and **XA3**, were synthesized by a one-pot domino-Oxa-Michael addition reaction, using cyclohexen-1-one and substituted hydroxybenzaldehydes, with the base 4-dimethylaminopyridine (DMAP) in ethanol for 24–48 h. **XA1** has been previously characterized [27], whereas the full spectroscopic characterization of **XA2** and **XA3**, is provided in **Section S1** (**Figs. S1** – **S6** of the Supplementary Materials). For **XA2**, the molecular ion peak at m/z 231.0997 $[M+H]^+$ in the HR-MS (ESI) spectrum corresponds to the molecular formula $C_{14}H_{14}O_3$, consistent with the ^1H and ^{13}C NMR spectra showing 14 proton and 14 carbon signals. Similarly, the structure of the repurposed compound **XA3** was confirmed by its molecular ion peak at m/z 216.08 $[M]^+$ in the GC-MS (EI) spectrum, matching the molecular formula $C_{13}H_{12}O_3$, and supported by the expected ^1H and ^{13}C resonance signals. In addition, the predicted physicochemical parameters and ADMET profiles for the xanthenone derivatives, indicating their drug-likeness and pharmacokinetic potential, are summarized in **Section S2**, **Table S1** of the Supplementary Materials.

Molecular characterization is essential to confirm the structural identity of the synthesized xanthenone derivatives. Although **XA3** has been previously reported, its solid-state structure has not been elucidated. This study presents the first single crystal X-ray diffraction (SC-XRD) analysis of the compound. The SC-XRD analysis verified structural purity, while Hirshfeld surface analysis reveals key intermolecular interactions that contribute to the molecular packing and overall stability of the compound [28, 29]. Yellow block crystals of **XA3** were obtained by slow ethanol evaporation. The molecular structure of the asymmetric unit of **XA3** is shown in Fig. 2A, with the superimposed enantiomeric arrangement illustrated in Fig. 2B. Detailed crystallographic information and refinement parameters are provided in **Table 1**, and additional geometry data are summarised in **Tables S2** and **S3** (Supplementary Material). The structure confirms that **XA3** is chiral, with a stereogenic centre at C9 (bonded to O2, sp^2-hybridised carbon C8, sp^3-hybridised carbon C13, and H9). Further analyses revealed that the

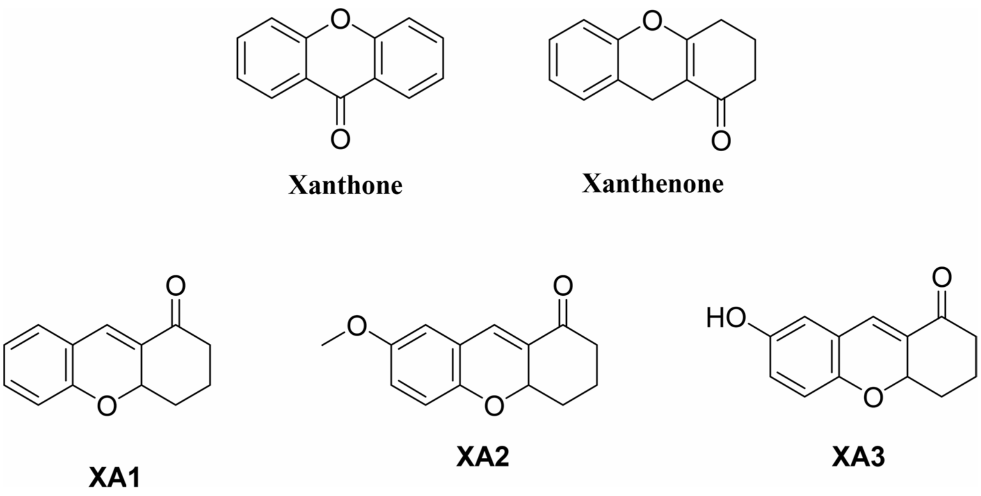

Fig. 1 General chemical structures of xanthone, xanthenone and their derivatives (XA1, XA2 and XA3)

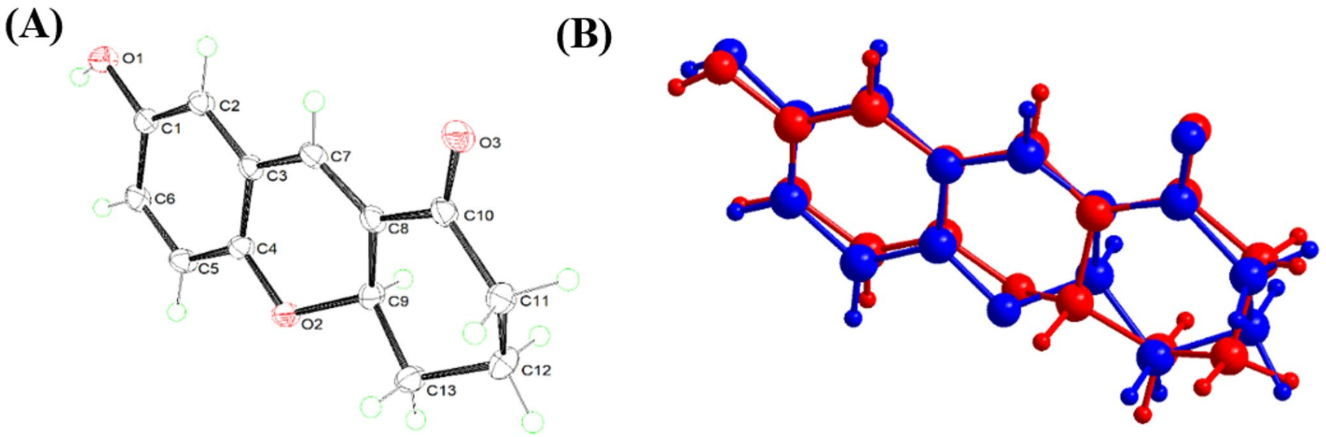

Fig. 2 Molecular structure of XA3. (**A**) Atom labelling scheme with anisotropic displacement parameters at 50% probability level. (**B**) Overlay of the XA3 enantiomer

Table 1 Crystal data and structure refinement for XA3

Compound	XA3	Compound	XA3
Formula	$C_{13}H_{12}O_3$	Z	4
Formula weight	216.23	ρ_{calc} (g cm^{-3})	1.409
Crystal size (mm^3)	0.223 × 0.070 × 0.044	μ (mm^{-1})	0.820
Crystal system	Monoclinic	*F* (000)	456.0
Space group	*P*2$_1$/*c*	Reflection	
a (Å)	7.60560(10)	Collected	12,854
b (Å)	6.83750(10)	Unique	2102
c (Å)	19.6893(4)	with $I>2\sigma(I)$	1964
α (°)	90	$R(F)$ [$I>2\sigma(I)$]	0.0389
β (°)	95.491(2)	No. parameters	150
γ (°)	90	$wR(F^2)$ [all data]	0.1103
Volume (Å^3)	1019.21(3)	max/min $\Delta\rho$ (e Å^{-3})	0.39/-0.24

sample exists as a racemic mixture, containing both enantiomers in a 1:1 ratio. Supplementary analyses of intermolecular contacts, supramolecular packing, and Hirshfeld surface features (d_{norm} maps and 2D fingerprint plots), are provided in **Figs. S7-S11** (**Section** S3 of Supplementary Material).

Evaluation of the Antifungal Effect of Xanthenone Series on Fluconazole-Resistant *C. auris*

A preliminary evaluation of the antibacterial efficacy of **XA1**, **XA2** and **XA3** was conducted against various pathogenic microorganisms, including those from oral, foodborne, aquatic and nosocomial sources, such as *Streptococcus* spp. and *Candida* spp. (**Section** S4, **Table** S4 in the Supplementary Material). Meanwhile, detailed antifungal studies of **XA1** were previously discussed by Ramli et al. (2024) [27]. At 100 µg/mL, **XA3** inhibited 52.08% of *C. auris*, while **XA2** showed no detectable inhibition. Neither compound inhibited *C. glabrata*, and both **XA2** and **XA3** exhibited low activity (<25% inhibition) against *C. albicans*.

The observed differential susceptibility suggests a substituent-dependent structure–activity relationship (SAR). **XA3** contains a free phenolic hydroxyl group, whereas **XA2** has a methoxy substituent. The hydroxyl group may enhance hydrogen-bonding capacity, polarity, and interactions with fungal cellular targets, consistent with reports highlighting the importance of hydroxy substituents in xanthone derivatives [64–65, 10]. In contrast, methoxy substitution may alter physicochemical properties such as lipophilicity and target engagement, potentially reducing antifungal potency. Thus, structural differences between **XA2** and **XA3** likely influence properties including polarity, hydrogen-bonding capacity, and membrane interaction, thereby affecting antifungal activity.

Species-specific biological factors may also contribute to variable susceptibility. *C. auris* has a thicker, chitin-rich cell wall that may allow selective permeation of polar compounds such as **XA3** [66, 67], whereas *C. glabrata* and *C. albicans*, which are known to influence antifungal sensitivity [66–69]. Differences in membrane composition, permeability, oxidative stress responses, and drug transport systems may therefore affect intracellular accumulation and activity of these compounds. Collectively, these findings suggest that both substituent-dependent SAR effects and species-specific fungal biology contribute to the observed differential activity of xanthenone compounds.

XA3 Effects on the Morphology, Structure and Membrane Permeability of *C. auris*

After determining the minimum inhibitory concentration (MIC: 100 µg/mL) and fungistatic profile of **XA3** (**Fig.** S12, **Section** S5 in Supplementary Material), field emission scanning electron microscopy (FE-SEM) was used to observe morphological and ultrastructural changes in *C. auris* following treatment with **XA3** at MIC and 2×MIC concentrations, as well as in control groups for comparison. Unlike the smooth, oval-shaped untreated cells (Fig. 3A), **XA3**-treated cells showed a roughened surface, constrictions and structural collapse, particularly evident at 2×MIC (Fig. 3C). At MIC, some cells retained normal morphology (Fig. 3B), but overall, similar destructive changes were observed at both concentrations. In comparison, fluconazole-treated cells showed milder surface damage without constriction (Fig. 3D). These similar morphological changes at MIC and 2×MIC strongly suggest that **XA3** disrupts the cellular integrity of *C. auris*, leading to membrane damage that likely causes leakage of cytoplasmic contents.

To support this hypothesis, the propidium iodide (PI)/fluorescein diacetate (FDA) [PI/FDA] uptake assay was performed to assess the effects of **XA3** on membrane permeability and cell viability in *C. auris*. PI selectively stains dead or damaged cells with compromised membranes, emitting red fluorescence, while FDA labels living cells with intact membranes and active metabolism, emitting green fluorescence [30]. Treatment of *C. auris* with **XA3** at MIC and 2×MIC significantly increased PI uptake (red fluorescence) and decreased FDA staining (green fluorescence), indicating increased membrane permeabilization and loss of cell viability, consistent with the morphological damage observed by FE-SEM. These fluorescence data (Fig. 4) quantitatively and visually confirm that membrane disruption induced by **XA3** leads to cytoplasmic leakage and cell death.

Effects of XA3 on ROS Production in *C. auris*

Excessive accumulation of reactive oxygen species (ROS) can cause DNA and RNA damage. To determine whether the inhibitory effect of **XA3** is related to ROS generation, intracellular ROS levels were measured using the H_2DCFDA assay. H_2DCFDA is a non-fluorescent probe that fluoresces upon reaction with ROS, enabling the quantification of oxidative stress. As shown in Fig. 5, both **XA3**-treated groups (MIC and 2×MIC) showed moderate green fluorescence, higher than the negative control but lower than the fluconazole-treated group (300 µg/mL, positive control). This signifies that although **XA3** induces oxidative stress in *C. auris*, it likely exerts its effects via additional mechanisms beyond ROS generation, compared to fluconazole. Furthermore, bright field (Fig. 5) and PI/FDA images support reduced cell density and membrane destruction in

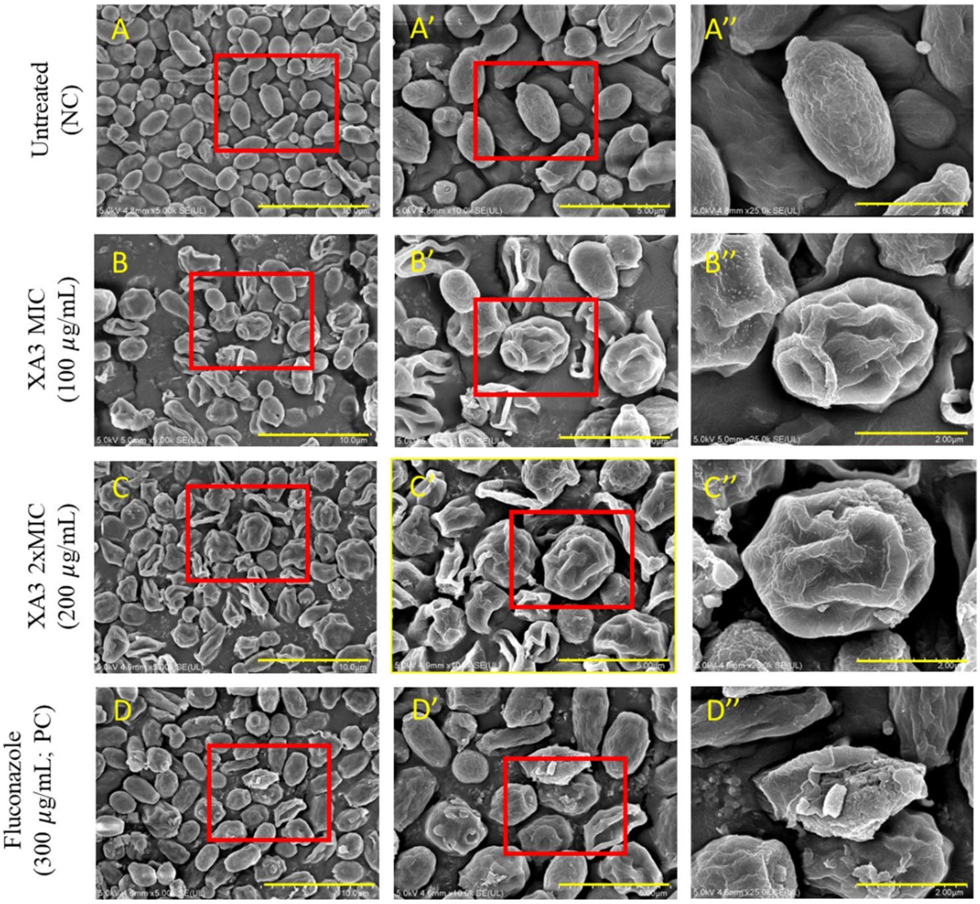

Fig. 3 Evaluation of morphological and structural changes by FE-SEM of cells treated with XA3. (**A**) Untreated cells (negative control), (**B**) cells treated with the MIC of XA3 (100 µg/mL), (**C**) cells treated with 2 × MIC of XA3 (200 µg/mL), and (**D**) cells treated with fluconazole (300 µg/mL; positive control). (**A'**-**D''**) Stepwise magnifications of (**A**-**D**). Scale bar = 10.0 µm. (**A**-**D**); 5.0 µm (**A'**-**D'**); 2.0 µm (**A''**-**D''**)

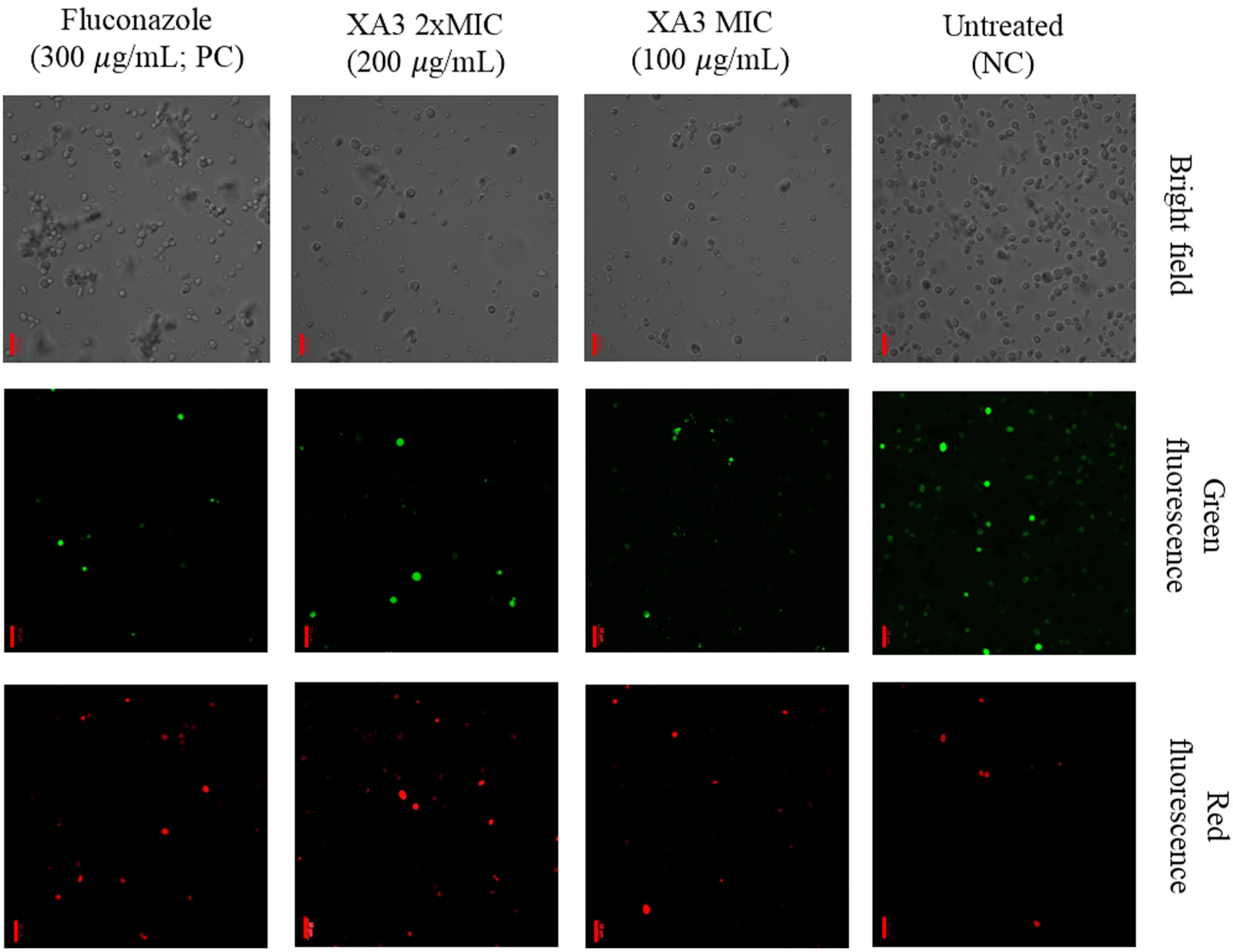

Fig. 4 Alterations in *C. auris* membrane permeability induced by XA3 in the PI/FDA uptake assay. Cells were exposed to PBS (negative control), XA3 at MIC and 2 × MIC, and fluconazole (300 µg/mL; positive control), then incubated at 37 °C for 10 h. Stained cells were visualized using the confocal laser scanning microscopy (CLSM) at excitation wavelengths of 535 nm and 617 nm, and emission wavelengths of 488 nm and 535 nm. Scale bar; 10 µm

XA3-treated cells, indicating a multifaceted mechanism. In contrast to fluconazole [31, 32], **XA3** appears to act primarily through structural damage and changes in membrane permeability over ROS generation, emphasising its potential as an antifungal agent.

Inhibition and Eradication of Biofilm Formation by XA3

Biofilm formation increases resistance to antimicrobial treatment by limiting drug penetration. To evaluate the effect of **XA3** on *C. auris* biofilm formation, the crystal violet (CV) staining method was used. **XA3** showed considerable biofilm inhibition at 50, 100 and 200 µg/mL, with inhibition rates of 43.56%, 62.19% and 66.78%, respectively (Fig. 6A). Remarkably, even at the lowest concentration of 50 µg/mL, **XA3** outperformed the positive control fluconazole at 300 µg/mL (29.74% inhibition). This suggests that the biofilm inhibitory effect of **XA3** is concentration dependent. Furthermore, the efficacy of **XA3** in eradicating pre-existing biofilms was similar to that of fluconazole. Eradication rates remained below 50% at all concentrations tested: 16.01% at 50 µg/mL, 34.36% at 100 µg/mL and 32.47% at 200 µg/mL. Interestingly, the biofilm eradication efficacy of **XA3** at 50 and 100 µg/mL was comparable to the positive control fluconazole (eradication rate of 34.85%; Fig. 6B). These findings indicate that **XA3** is particularly more effective in preventing biofilm development than in eradicating established biofilms and thus offers a strategic approach to controlling *C. auris* infections in their early stages.

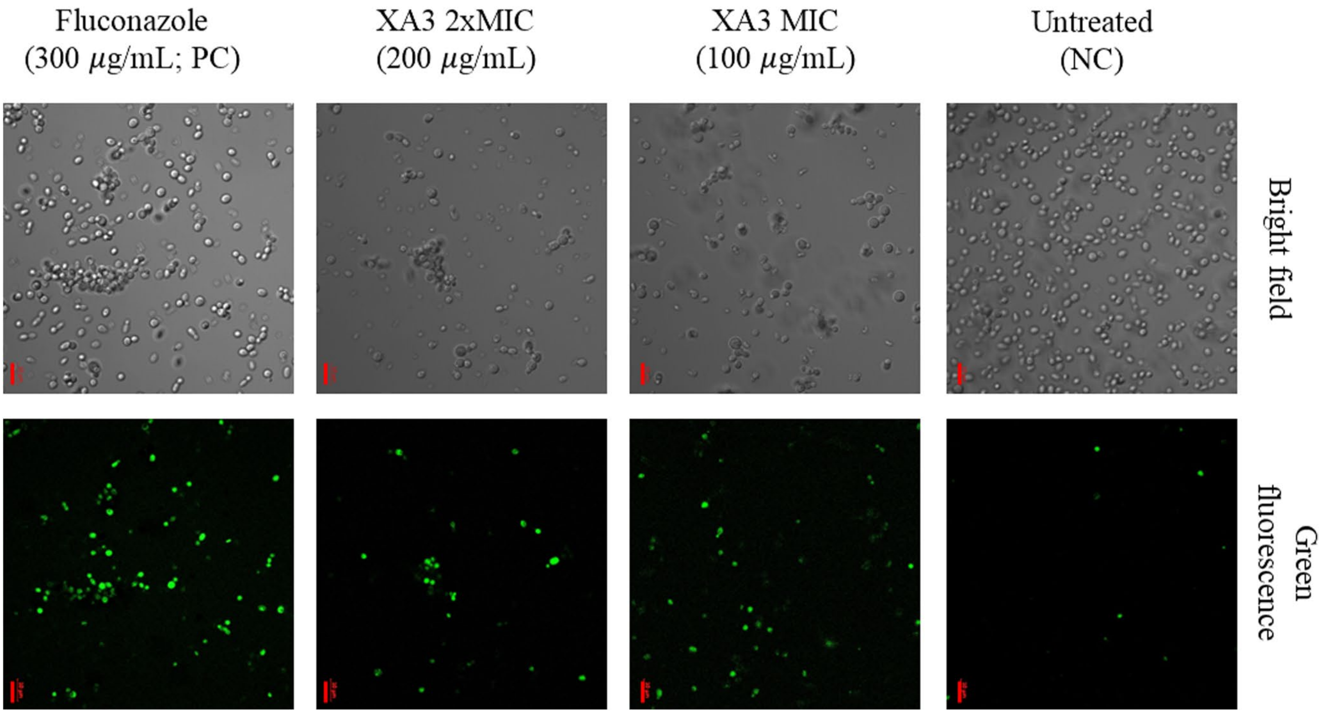

Fig. 5 ROS generation in *C. auris* induced by XA3. CLSM bright field and fluorescence images show ROS production in *C. auris* treated with fluconazole (300 µg/mL; positive control), XA3 (MIC and 2 × MIC), and PBS (negative control). At excitation and emission wavelengths of 488 nm and 535 nm, respectively, green fluorescence was detected in fungal cells stained with H_2DCFDA and observed by CLSM. Scale bar: 10 µm

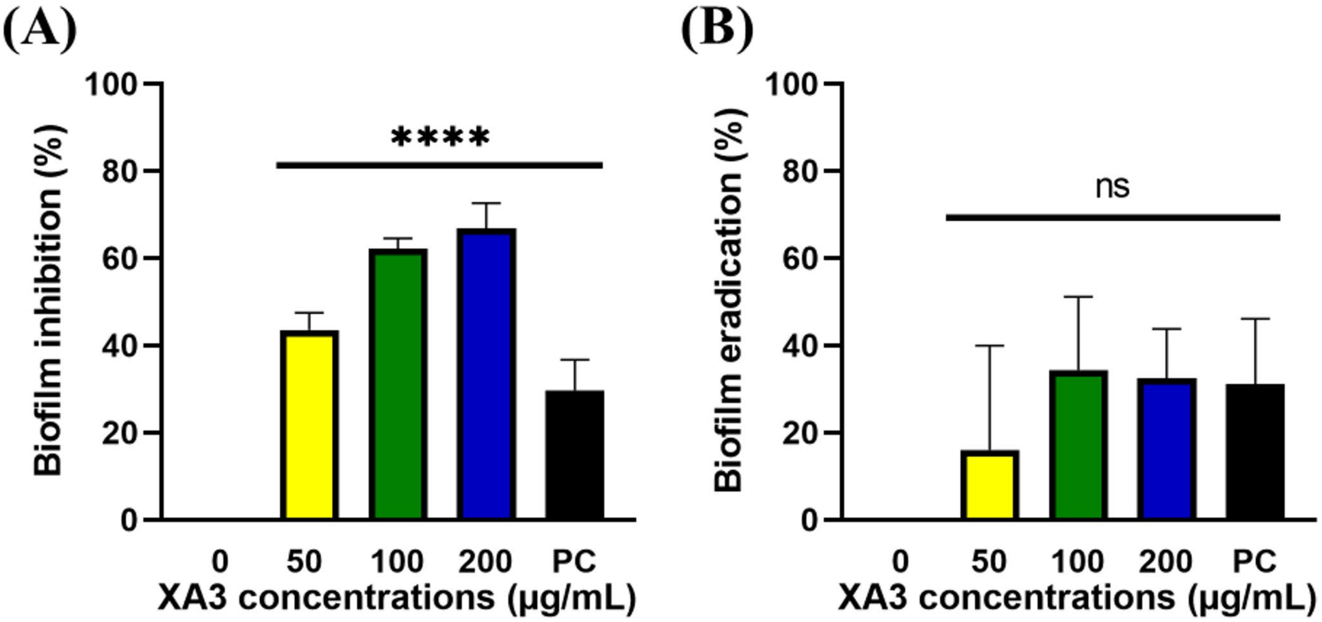

Fig. 6 Quantitative assessment of biofilm (**A**) inhibition and (**B**) eradication of XA3 in *C. auris*. Increasing concentrations of XA3 (0–200 µg/mL) were used in both assays, with fluconazole (300 µg/mL) as the standard drug (PC: positive control). After treatment with XA3, the biofilm adhering to the wall surface was stained with CV and quantified by measuring OD_{595}. Statistical significance is denoted by $^{****}p < 0.0001$, indicating a significant difference compared to the negative control, while 'ns' indicates no significant difference in biofilm eradication. Error bars represent the mean ± SD (n = 3)

The CV staining showed that **XA3** effectively inhibits and eradicates biofilms of *C. auris*. Biofilm-associated infections are clinically challenging due to their protective matrix, which increases microbial resistance by up to 1,000-fold [33, 34]. *C. auris* readily forms robust biofilms on medical devices (such as catheters, heart valves and joint prostheses) and tissues, contributing to persistent infections with high morbidity [34]. This resistance stems from limited drug penetration, an altered microenvironment and the presence of persister cells, often necessitating prolonged therapy or removal of the device [35, 36].

XA3 shows a strong inhibitory effect on *C. auris* biofilm formation, comparable to fluconazole, highlighting its potential as a preventive antifungal. While its activity against mature biofilms is limited, its primary strength is in preventing biofilm development, which is crucial for treating infections associated with medical devices. In antifungal treatment protocols, **XA3** could be particularly valuable for prophylaxis or as part of combination therapy, preventing initial colonisation while other agents target established biofilms [37–39]. This dual strategy approach could improve treatment outcomes and help reduce resistance to fungal infection by reducing persistent infections.

To further substantiate the antifungal mechanisms of **XA3**, the expression of key virulence genes in *C. auris* was analyzed after treatment with its MIC (**Section S6** and **Table S5** in the Supplementary Material). **XA3** downregulated genes related to drug resistance (*cdr1* and *mdr1*), redox homeostasis (*cat1*), hyphae formation (*hyr1*) and protein folding (*sti1*) compared to the PBS control (**Fig. S13** in the Supplementary Material). Notably, expression of *cdr1* remained near baseline with **XA3** (0.90-fold) but was upregulated by fluconazole (1.91-fold), suggesting that **XA3** may better circumvent common resistance mechanisms and provide therapeutic benefits.

In Vitro Toxicity Analysis of XA3 on HaCaT and B16F10 Cultured Cells

In vitro cytotoxicity assessment using human HaCaT keratinocytes and B16F10 murine melanoma cells was conducted to confirm the selective safety of **XA3** and to ensure that its antifungal and depigmenting effects were not due to nonspecific cytotoxicity. Confirmation of cytocompatibility with both skin and pigment-producing cells supports the potential therapeutic use of **XA3**, particularly for treating skin-related *C. auris* infections and pigmentation disorders.

The cytotoxic effects of **XA3** on HaCaT keratinocyte cells were assessed using the MTT assay at different concentrations: 6.25 μg/mL (90.45% viability), 12.5 μg/mL (91.61% viability), 25 μg/mL (85.04% viability) and 50 μg/mL (73.69% viability) (Fig. 7A). Although a statistically significant reduction in cell viability was observed at all concentrations compared to the negative control, viability remained above 80% at concentrations up to 25 μg/mL. indicating low cytotoxicity according to ISO 10993-5 guidelines [40, 41]. At 50 μg/mL, viability decreased to 73.69%, indicating mild cytotoxicity. These results support the safety of **XA3** at lower concentrations and highlight the importance of optimizing the balance between cytocompatibility and antifungal efficacy.**XA3** also showed strong antifungal activity against fluconazole-resistant *C. auris*, particularly by inhibiting biofilm formation at 50 μg/mL, outperforming fluconazole at 300 μg/mL. Although effective, defining a clear therapeutic window is critical to ensure host cell safety. The higher MIC required for *C. auris* likely reflects its resilient cell wall and drug-resistant characteristics, underscoring the need for dose optimization in the further development of **XA3**.

The cytotoxicity of **XA3** in B16F10 melanoma cells was tested at concentrations ranging from 1.56 to 50 μg/mL,

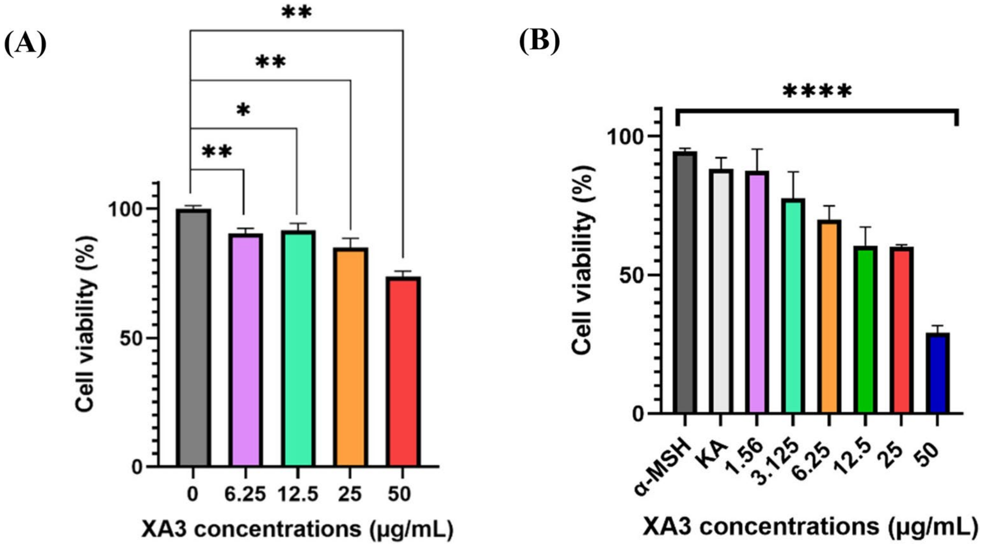

Fig. 7 MTT-based cytotoxicity analysis of XA3 on (**A**) HaCaT and (**B**) B16F10 cells. Untreated cells served as control groups (α-MSH-induced for B16F10). XA3 treatments at different concentrations (HaCaT: 6.25–50 μg/mL; B16F10: 1.56–50 μg/mL) decreased cell viability after 24 h. Kojic acid (7.10 μg/mL) was included as a reference in (**B**). Cell viability was measured at (**A**) OD_{595} and (**B**) OD_{570} and expressed as mean ± SD ($n = 3$). Statistical significance: $^{*}p < 0.05$, $^{**}p < 0.005$, $^{****}p < 0.0001$

following pre-treatment with 200 nM α-melanocyte stimulating hormone (α-MSH) to maintain melanogenic activity. As shown in Fig. 7B, **XA3** induced a dose-dependent reduction in cell viability, decreasing from 87.56% (at 1.56 µg/mL) to 29.19% (at 50 µg/mL). In comparison, kojic acid (7.10 µg/mL) caused only a slight decrease in viability. The higher sensitivity of B16F10 cells compared to HaCaT cells to **XA3**, particularly above 12.5 µg/mL, is likely due to active melanin synthesis and tyrosinase expression, which metabolize **XA3** into reactive intermediates that trigger redox cycling and Fenton reactions, increase intracellular ROS levels and induce oxidative stress-related cell death [42]. In contrast, HaCaT cells lack tyrosinase and produce less ROS, suggesting that **XA3** acts via a selective pro-oxidant mechanism that targets melanocytic cells while sparing normal keratinocytes.

Altogether, the selective cytotoxicity of **XA3** suggests a favourable therapeutic window and shows efficacy against *C. auris*, inhibition of melanocyte activity in B16F10 cells, and safety in normal skin cells. The relatively low cytotoxicity in HaCaT cells at the biofilm inhibitory concentration (50 µg/mL) suggests a measurable safety margin for antifungal testing conditions. To further investigate the other bioactivity, anti-melanogenesis and anti-tyrosinase assays were performed in vitro on α-MSH-induced B16F10 cells and in vivo using zebrafish.

In Vivo Toxicity Tests of XA3 Effects in Zebrafish Animal Model

To validate the anti-melanogenic potential of **XA3** and assess its biosafety in the whole organism, in vivo studies were performed using zebrafish. This approach offers a complementary platform to cellular assays and enables the evaluation of developmental and pigmentation outcomes in a physiologically relevant system. Zebrafish embryos and larvae, up to 5 days post-fertilization (dpf), provide a cost-effective and ethical alternative for animal studies that supports the 3Rs (Replacement, Reduction, and Refinement) guidelines [48]. Their exceptional transparency allows direct observation of pigmentary changes and developmental effects [49–52], while whole-organism assessment accounts for pharmacokinetic factors such as absorption and distribution [53]. With 84% genetic homology to humans, including conserved pigmentation genes (*mitf*, *tyr*, *tyrp1*) and signalling pathways (PI3K, cAMP/PKA, MAPK) [51, 53, 54], zebrafish offer greater translational relevance for evaluating melanogenesis inhibitors compared to cellular models. This complementary platform bridges the gap between in vitro assays and mammalian studies, providing comprehensive efficacy and safety data in a living system.

In this study, the in vivo activity of **XA3** was evaluated by exposing zebrafish embryos at the gastrulation stage (6 hpf) to various concentrations (12.5, 6.25, 3.125, 1.5 and 0.7 µg/mL), with morphological observations conducted up to 72 hpf. The results showed that the median lethal dose (LD_{50}) of **XA3** was 6.25 µg/mL (**Fig. S14** in Supplementary Material). Concentrations above 12.5 µg/mL were not used in zebrafish experiments as the preliminary testing showed severe acute toxicity, with near-complete mortality at 24 hpf and an estimated LD_{50} of approximately 6.25 µg/mL. Therefore, lower sublethal concentrations were selected for in vivo evaluation. Prolonged exposure to **XA3** at sublethal concentrations of 3.125 and 1.5 µg/mL produced visible anti-melanogenic effects at 48 hpf, whereas embryos exposed to the lowest concentration (0.7 µg/mL) showed no changes in pigmentation (Fig. 8). Based on these findings, the effects of **XA3** on vascular development were assessed using a blood vessel-specific transgenic zebrafish embryo [*Tg(kdrl: egfp)*], which expresses green fluorescent protein (GFP) in vascular endothelial cells [55]. These embryos were treated with **XA3** (3.125, 1.5 and 0.7 µg/mL) at 10 hpf and analyzed at 30 hpf. While the lowest concentration (0.7 µg/mL) had no observable effect on vascular development, higher concentrations (3.125 and 1.5 µg/mL) induced structural alterations in the intersegmental vessels (ISVs) of both trunk and head regions, indicating a concentration-dependent effect on angiogenesis (Fig. 9A).

To determine whether the observed anti-melanogenic and anti-angiogenic effects were associated with general cytotoxicity, AO staining was performed at 72 hpf to detect apoptotic cells in embryos treated with **XA3** (3.125, 1.5 and 0.7 µg/mL). Apoptosis, characterised by distinct

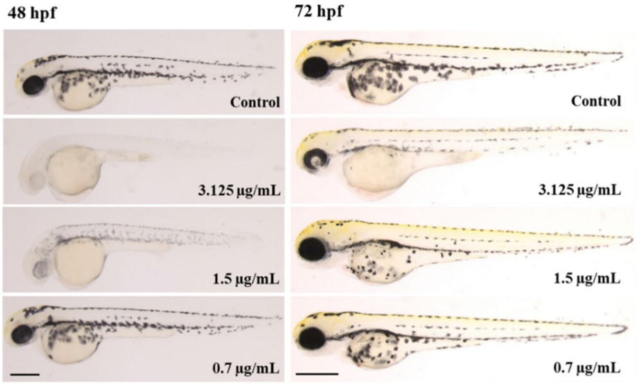

Fig. 8 Effects of XA3 on melanogenesis in zebrafish larvae. Representative lateral views (anterior to the left) of zebrafish larvae treated with XA3 at different concentrations (0.7, 1.5, and 3.125 µg/mL) and corresponding controls at 48 hpf (left panel) and 72 hpf (right panel). XA3 exhibited anti-melanogenic effects at 3.125 µg/mL and 1.5 µg/mL, while no significant change in pigmentation was observed at 0.7 µg/mL compared with the control groups. Five larvae were analyzed per concentration. Scale bar: 200 µm

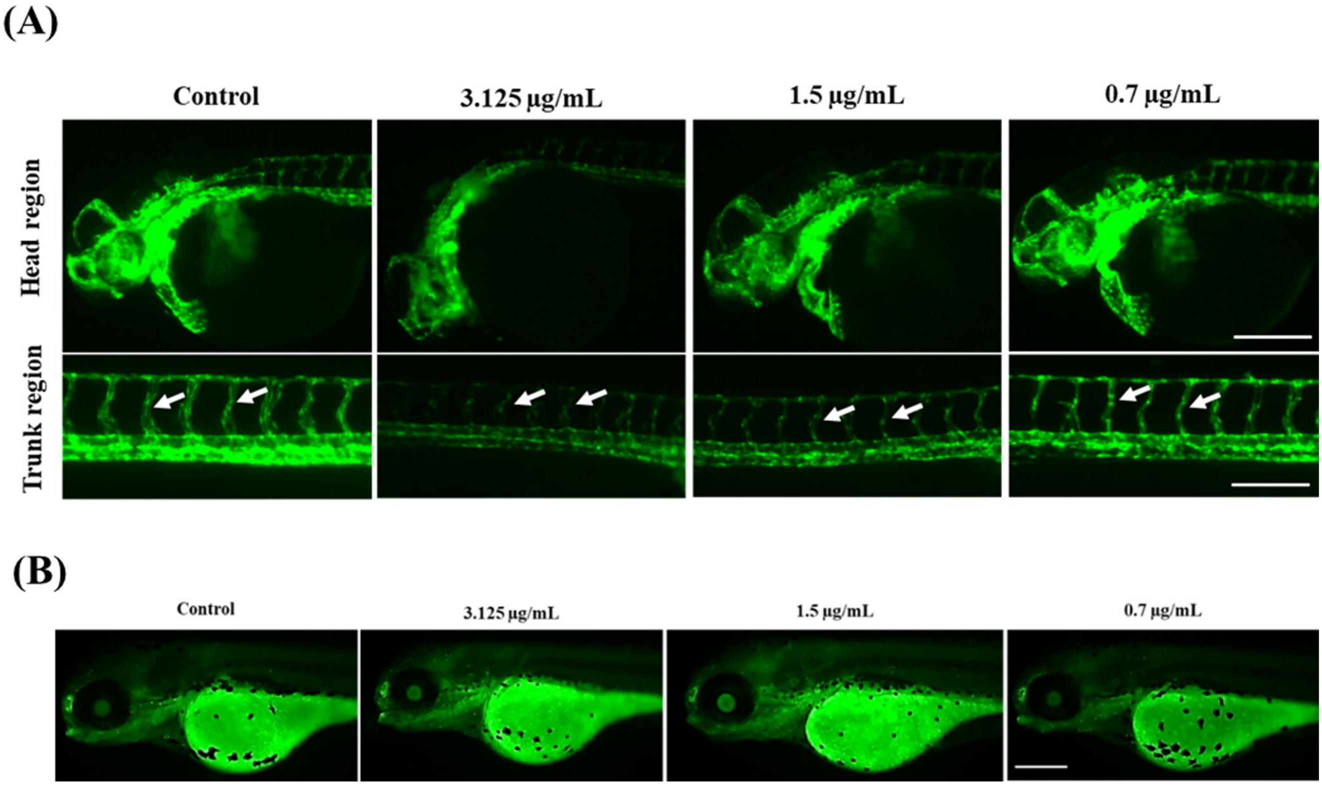

Fig. 9 Evaluation of vascular development and cellular apoptosis in zebrafish embryos following XA3 exposure. (**A**) Effects on angiogenesis in the transgenic *Tg[kdrl: egfp]* line at 30 hpf. Representative fluorescence images of the head and trunk vasculature show that XA3 treatment at 1.5 µg/mL and 3.125 µg/mL impairs intersegmental vessel (ISV) formation (white arrows) and reduces head vasculature, while no impairment is observed at 0.7 µg/mL. (**B**) Assessment of cell death by acridine orange (AO) staining. Representative fluorescence images show no significant increase in AO-positive cells in XA3-treated groups compared to the control, indicating a lack of pro-apoptotic activity at the tested concentrations. Note: Bright green fluorescence in the yolk region is due to natural autofluorescence. Each condition was validated using three embryos per concentration. Scale bar: 200 µm

morphological features such as cell shrinkage, membrane blebbing and chromatin condensation [56], was not detected at any of the concentrations tested (Fig. 9B). The absence of detectable apoptosis suggests that the vascular and pigmentation phenotypes are not attributable to widespread cytotoxicity. However, given the observed anti-angiogenic activity, these findings indicate biologically specific effects that require further mechanistic investigation to clarify their underlying pathways, safety implications, and relevance for future pharmacological optimisation [70, 71].

Collectively, cytotoxicity assays in HaCaT keratinocytes, B16F10 melanoma cells, and zebrafish embryos showed that **XA3** is well tolerated at sub-inhibitory concentrations, although these concentrations are below the MIC (100 µg/mL) required for antifungal activity against *C. auris*. The MIC of **XA3** against *C. auris*, together with cytotoxicity observed at lower concentrations, indicates a limited therapeutic window in its current form. Therefore, **XA3** is not proposed as a standalone antifungal but should be considered an early-stage hit requiring further optimization. Such efficacy and safety profiles are common in discovery-stage compounds and can be improved through rational structural modification [72, 73]. In addition, **t**opical delivery strategies and combination approaches of **XA3** with existing antifungals may improve therapeutic feasibility by reducing the effective concentration required [74, 75].

On the other hand, this suggests that the available safety data are more relevant for anti-melanogenic than antifungal use, highlighting the need for further studies to define the therapeutic window at fungicidal doses. Importantly, the antifungal and anti-melanogenic effects of **XA3** occur at different concentration ranges and through different mechanisms: (1) the antifungal effect at the MIC is due to membrane disruption and fungal cell death, while (2) the anti-melanogenic effects at lower, sublethal doses result from inhibition of melanin biosynthesis, including suppression of tyrosinase. This concentration-dependent distinction indicates that the antifungal and anti-melanogenic activities of **XA3** occur within distinct pharmacological ranges.

Evaluation of Anti-Melanogenic Efficacy in B16F10 Cells and Zebrafish Embryos

The anti-melanogenic efficacy of **XA3** was evaluated using a dual-model approach involving α-MSH-stimulated B16F10 melanoma cells and zebrafish embryos to replicate physiological hyperpigmentation. In the B16F10 cell model, α-MSH stimulation successfully established a hyperpigmented state [43], increasing melanin content and tyrosinase activity to 100%. **XA3** treatment produced a potent, dose-dependent inhibitory effect, reducing melanin content to 85%, 42%, and 13% at concentrations of 1.56, 6.25, and 25.0 µg/mL, respectively (Fig. 10A.**I**). This performance was highly comparable to the benchmark inhibitor, kojic acid (6% melanin). Similar results were observed in the anti-tyrosinase assay (Fig. 10A.**II**), where **XA3** suppressed enzymatic activity to as low as 5% at the highest dose. These concurrent reductions suggest that **XA3** inhibits melanogenesis through direct suppression of tyrosinase, likely via competitive enzymatic inhibition or protein downregulation, rather than through indirect antioxidant pathways [25, 44–47].

This mechanistic profile was further validated in vivo using the zebrafish model. To ensure accurate visualization, embryos were pre-treated with 1-phenyl-2-thiourea (PTU) to establish a transparent baseline before α-MSH stimulation

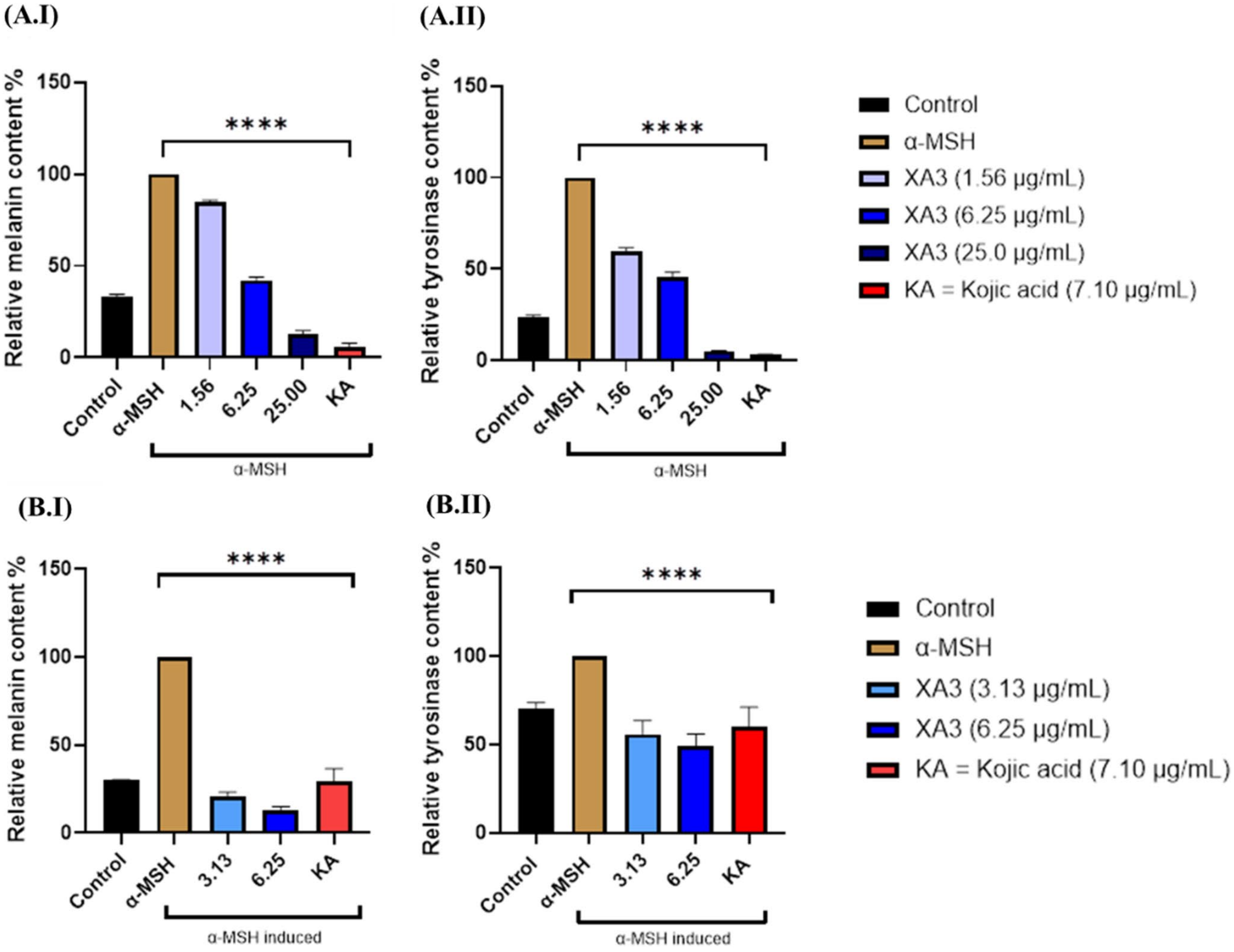

Fig. 10 Comprehensive anti-melanogenic evaluation of XA3 using in vitro and in vivo models. (**A**) Effects in B16F10 murine melanoma cells stimulated with α-MSH; (**A.I**) Relative melanin content and (**A.II**) tyrosinase activity demonstrate dose-dependent inhibition by XA3, with the 25.0 µg/mL dose showing activity comparable to the kojic acid (KA) standard. (**B**) In vivo evaluation in zebrafish embryos at 48 hpf; (**B.I**) Relative melanin content shows that XA3 significantly reduces pigmentation, outperforming the KA control at the 6.25 µg/mL concentration. (**B.II**) Relative tyrosinase levels indicate potent suppression of the key melanogenic enzyme, comparable to KA. All data are expressed as relative percentages compared to α-MSH-stimulated controls. Error bars represent mean ± SD (****$p < 0.0001$)

[57, 58]. Microscopic examination revealed a pronounced depigmenting effect in **XA3**-treated embryos (see **Fig. S15** in Supplementary Material). As shown in Fig. 10B.**I**, quantitative analysis confirmed that **XA3** (6.25 µg/mL) reduced melanin content to 13%, significantly outperforming the kojic acid control (30%) within its non-toxic range (LD_{50} = 6.25 µg/mL). Furthermore, **XA3** reduced in vivo tyrosinase levels to 49%, exceeding the 60% inhibition achieved by kojic acid (Fig. 10B.**II**). The strong correlation between the in vitro B16F10 data and the in vivo zebrafish results confirms that tyrosinase suppression is the primary mode of action for **XA3**. By demonstrating greater potency than kojic acid in an organismal model, **XA3** emerges as a promising candidate for the treatment of pigment-related disorders and the development of innovative dermatological therapeutics.

Conclusion

In summary, **XA3** is a promising dual-function xanthenone derivative with significant antifungal and anti-melanogenic properties. The 7-hydroxy (-OH) group in **XA3** is critical for its enhanced bioactivity, as it increases hydrogen bonding, polarity, membrane interaction, ROS modulation, and direct enzyme inhibition compared to the unsubstituted (**XA1**) and methoxy-substituted (**XA2**) analogues. Against *C. auris*, **XA3** inhibited fungal growth and biofilm formation with an MIC of 100 µg/mL. Time-kill kinetics confirmed a primarily fungistatic effect, associated with structural damage, membrane disruption, induction of ROS and inhibition of biofilm formation. In addition, **XA3** showed significant anti-melanogenic effects by reducing melanin content and tyrosinase activity in α-MSH-stimulated B16F10 melanoma cells in a dose-dependent manner, surpassing the efficacy of kojic acid. These results were further validated in zebrafish embryos, which possess conserved melanogenesis pathways. This concentration-dependent bioactivity demonstrates that **XA3** exhibits pharmacologically distinct antifungal and anti-melanogenic effects. These findings position **XA3** as a bioactive hit scaffold that warrants further structural optimization to enhance potency and improve safety margins. Future pharmacological investigations are necessary to better define its mechanistic profile and therapeutic relevance.

Experimental

Chemistry

Following the domino oxa-Michael addition procedure, a mixture of 4-dimethylaminopyridine (DMAP; 1 mmol) and substituted hydroxybenzaldehydes (5 mmol) was added to cyclohexen-1-one (10 mmol) in 10 mL of ethanol **(**Scheme 1**)** for preparation of the **XA** series. The reaction mixture was stirred at room temperature for 48 h, or until the hydroxybenzaldehydes had fully reacted. The mixture was then acidified with dilute hydrochloric acid (HCl) solution and quenched with ice water. The resulting precipitate was dried in vacuo, filtered, and rinsed with water or extracted with ethyl acetate (3 × 10 mL). All crude products were purified by preparative TLC in hexane: ethyl acetate (4:1), recrystallized from ethanol and spectroscopically analyzed by ^{1}H and ^{13}C nuclear magnetic resonance (NMR) and high-resolution mass spectrometry (HR-MS) for structural characterization. All compounds were confirmed to be > 95% pure by ^{1}H NMR and GC-MS analyses, with no detectable impurities. The corresponding NMR and GC-MS spectra are provided in **Section S1**, **Figs. S1-S6** in the Supplementary Material. After purification, the **XA** compounds were prepared with distilled water and 10% DMSO at concentrations of 1 mg/mL and 2 mg/mL for subsequent in vitro antimicrobial assays.

2,3,4,4a-Tetrahydro-1H-xanthen-1-one (**XA1**). Following the general synthetic procedure, DMAP (1 mmol) was reacted with 2-hydroxybenzaldehydes (5 mmol) in 10 mL ethanol, before the addition of cyclohexen-1-one (10 mmol). The reaction proceeded for 24 to 48 h at room temperature, and the product was purified and recrystallized to afford a pale-yellow crystal. Yield: 65%; mp: 116–118 °C; Spectroscopic data including ^{1}H NMR, ^{13}C NMR and GCMS have been reported [27].

7-Methoxy-2,3,4,4a-tetrahydro-1H-xanthen-1-one (**XA2**). Following the general synthetic procedure, DMAP (1 mmol) was first reacted with 2-hydroxy-5-methoxybenzaldehyde (5 mmol) in 10 mL ethanol, before cyclohexen-1-one (10 mmol) was added. The reaction mixture was stirred continuously at room temperature for 24 to 48 h, then purified and recrystallized to obtain the product

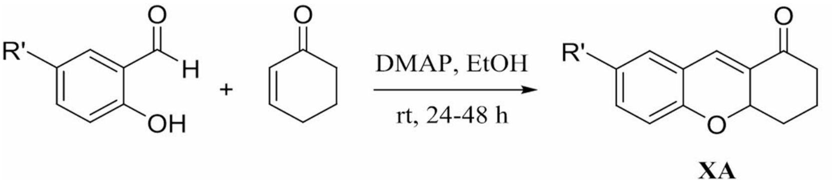

R'	Compound
H	XA1
OCH_3	XA2
OH	XA3

Scheme 1 Synthetic pathway for the preparation of tetrahydro-1*H*-xanthen-1-ones (XA1, XA2 and XA3)

as bright yellow crystals. Yield: 53%; mp: 116–118 ◦C; ^{1}H NMR (500 MHz, DMSO-d_6) δ: 7.33 (d, *J* = 2.4 Hz, 1H), 7.02 (d, *J* = 2.9 Hz, 1H), 6.89–6.75 (m, 2 H), 4.92 (ddd, *J* = 10.7, 6.0, 2.4 Hz, 1H), 3.69 (s, 3 H), 2.43–2.25 (m, 3 H), 1.96–1.80 (m, 2 H), 1.72–1.58 (m, 1H); ^{13}C NMR (125 MHz, DMSO-d_6) δ: 197.2, 154.5, 149.7, 131.9, 130.5, 122.9, 118.3, 116.8, 114.2, 74.7, 56.2, 55.9, 38.9, 29.4, 19.7, 17.7 ppm; HRMS (ESI): m/z calculated for $C_{14}H_{14}O_3$ is 231.0997 $[M+H]^+$.

7-Hydroxy-2,3,4,4a-tetrahydro-1H-xanthen-1-one (**XA3**). Following the general synthetic procedure, DMAP (1 mmol) was reacted with 2,5-dihydroxybenzaldehyde (5 mmol) in 10 mL ethanol, before cyclohexen-1-one (10 mmol) was added. The reaction mixture was stirred at room temperature for 24 to 48 h, then purified and recrystallized to collect the product as bright orange crystals. Yield: 60%; mp: 120–122 ◦C; ^{1}H NMR (500 MHz, DMSO-d_6) δ: 9.18 (s, 1H), 7.27 (d, *J* = 2.4 Hz, 1H), 6.76 (d, *J* = 2.8 Hz, 1H), 6.71 (d, *J* = 8.7 Hz, 1H), 6.67 (dd, *J* = 8.7, 2.8 Hz, 1H), 4.86 (ddd, *J* = 10.7, 6.0, 2.4 Hz, 1H), 2.41–2.27 (m, 3 H), 1.95–1.78 (m, 2 H), 1.71–1.53 (m, 1H); ^{13}C NMR (125 MHz, DMSO-d_6) δ: 197.1, 152.4, 148.5, 131.7, 130.7, 122.9, 119.2, 116.7, 115.6, 74.6, 38.9, 29.4, 17.7. GCMS (EI): m/z found for $C_{13}H_{12}O_3$ is 216.15 [M]+; 160.08.

X-ray Crystallography of XA3

Yellow blocky crystals of **XA3** were obtained via slow evaporation of the ethanolic solvent containing the compound. X-ray diffraction data were collected at 100 K using a Rigaku/Oxford Diffraction XtaLAB Synergy diffractometer (Dualflex, AtlasS2) with CuKα radiation ($\lambda = 1.54178$ Å). Data collection achieved 100% completeness up to $\theta = 67.7°$ and was subjected to standard reduction procedures, including absorption correction with CrysAlisPro [59]. The structure was solved using the direct dual-space methods implemented in ShelXT [60]. Subsequent refinement was performed against F^2, incorporating anisotropic displacement parameters and placement of C-bonded H atoms using a riding model approximation [60]. A weighting scheme of $w = 1/[\sigma^2(F_o^2) + (0.052P)^2 + 0.414P]$, where $P = (F_o^2 + 2F_c^2)/3$, was used in the final stages of refinement. The molecular structure diagram was generated using ORTEP3 for Windows [61] with 50% probability ellipsoids. Further analysis of the crystal packing was performed using PLATON [60]. The crystal data and refinement details are summarised in **Table 1**. The crystallographic data for **XA3** have also been deposited with the Cambridge Crystallographic Data Centre (CCDC) under the supplementary publication number CCDC 2,361,502. Free access to this data is available at https://www.ccdc.cam.ac.uk/.

In Vitro Antifungal Evaluation

Ultra Structural, Morphological and Membrane Permeability Changes of XA3 Treated *C. auris*: FE-SEM Analysis and PI/FDA Staining Assay

FE-SEM was used to assess the ultrastructural effects of **XA3** on *C. auris* at MIC and 2×MIC concentrations after a 10-hour incubation. Fluconazole (300 µg/ml) and untreated cells served as positive and negative controls, respectively. Morphological changes were analysed after the cells were washed, dehydrated and platinum coated. The effects of **XA3** on the membrane permeability of *C. auris* were then evaluated using PI/FDA staining assays. FDA indicates cell viability by turning green when metabolized by living cells, while PI stains dead cells red due to damaged membranes [27].

Effects of XA3 on the Reactive Oxygen Species (ROS) Production in *C. auris*: H_2DCFDA Staining Assay

Initially, *C. auris* cells (1×10^6 CFU/mL) were exposed to **XA3** at MIC and 2×MIC, then stained with 100 µg/mL 2′,7′-dichlorodihydrofluorescein diacetate (H_2DCFDA) and incubated in the dark for 30 min. After excess dye was removed, ROS production was quantified using a fluorescence spectrophotometer with excitation and emission wavelengths set to 488 nm and 535 nm, respectively [27].

Evaluation of the Effect of XA3 on Biofilm Formation Inhibition and Eradication

The inhibition of biofilm formation in *C. auris* was investigated by exposing cultures to varying concentrations of **XA3** (0–200 µg/mL) and incubating them for 24 h. For the biofilm eradication assay, preformed biofilms were treated with **XA3** (0–200 µg/mL) or fluconazole (300 µg/mL) and then incubated for 24 h. After staining with crystal violet, the absorbance of the biofilm was measured at 595 nm and the percentage of biofilm inhibition and eradication was calculated using the equation [27]:

$$\text{Biofilm inhibition or eradication (\%)} = \frac{\text{Absorbance untreated-Absorbance treated}}{\text{Absorbance untreated}} \times 100\%$$

In Vitro Cytotoxicity Assessment of XA3 in HaCaT and B16F10 Cells

The in vitro cytotoxicity of **XA3** was assessed at concentrations ranging from 1.56 to 50 µg/mL using HaCaT keratinocytes and B16F10 melanoma cells. HaCaT and B16F10 cells were seeded in 96-well plates at densities of 1×10^4 cells/mL and 2×10^5 cells/mL, respectively, and incubated at 37 °C with 5% CO_2 for 24 h. Following treatment with **XA3**, MTT solution (5 mg/mL) was added and incubated for 4 h. DMSO was then added to dissolve the formazan crystals. Absorbance was measured at 595 nm using a microplate reader (Bio-Rad, USA) and cell viability was calculated using the equation [27]:

$$\text{Cell viability (\%)} = \frac{\text{Absorbance treated cells}}{\text{Absorbance untreated cells}} \times 100\%$$

Anti-Melanogenic Assessment of XA3

In Vitro Evaluation of Anti-Melanogenesis and Anti-Tyrosinase of XA3 on B16F10 Melanoma Cells

To evaluate anti-melanogenic activity, B16F10 melanoma cells were seeded in 6-well plates at a density of 2×10^5 cells/well. After a 24-h incubation, the cells were treated with different concentrations of **XA3** (1.15, 6.25 and 25.0 µg/mL) along with 1 µM α-MSH to stimulate melanogenesis. After a further 24 h, the cells were rinsed with PBS and lysed with 1 N NaOH. The lysates were transferred to a 96-well plate and incubated at 90 °C for 1 h. Absorbance was then measured at 405 nm using a microplate reader (Bio-Rad, USA) [62], and melanin content was quantified relative to the untreated control using the equation:

$$\text{Relative melanin content (\%)} = \frac{\text{Absorbance treated cells}}{\text{Absorbance untreated cells}} \times 100\%$$

Meanwhile, for the anti-tyrosinase activity assay, B16F10 cells were seeded at 2×10^5 cells/well and first stimulated with 1 µM α-MSH to induce melanogenesis, followed by incubation for 24 h. The cells were then treated with different concentrations of **XA3** (1.15, 6.25 and 25.0 µg/mL) and incubated for another 24 h. Subsequently, the cells were washed with PBS, detached with TrypLE (1 ×) and incubated for 5 min. The cells were then collected, washed with PBS and lysed with a cold lysis buffer consisting of 10 mM sodium phosphate (pH 6.8), 1% Triton X-100 and 1 mM PMSF. The lysates were homogenised, and the supernatants were transferred to a 96-well plate. Tyrosinase activity was induced by the addition of L-DOPA and incubated for 15 min. The resulting dopachrome formation was quantified by measuring the absorbance at 450 nm using a microplate reader [62]. Tyrosinase activity was expressed as a percentage relative to the untreated control using the equation:

$$\text{Relative tyrosinase activity (\%)} = \frac{\text{Absorbance treated cells}}{\text{Absorbance untreated cells}} \times 100\%$$

In Vivo Assessment of XA3 Using the Zebrafish Animal Model

Zebrafish Husbandry and Embryo Collection

Wild-type zebrafish (*Danio rerio*) and a blood vessel-specific transgenic reporter line [*Tg*(*kdrl: egfp*)] were maintained under standardized laboratory conditions at our animal facility. All procedures involving live animals were conducted in accordance with the ethical guidelines approved by the Institutional Animal Care and Use Committee (IACUC) of Chungnam National University (Approval No. 202404 A-CNU-077). Adult zebrafish were kept in 2-liter tanks at a controlled temperature of 28 °C, following a 10-hour dark and 14-hour light photoperiod. They were fed three times daily alternating between freshly harvested brine shrimp (Artemia nauplii) from Inve Aquaculture, Inc. (Salt Lake City, UT, USA) and commercial flake food from Gemma Micro 75 zf, Skretting France, (Le Pont de Pierre, France). The aquatic system was supported by a continuous water circulation mechanism to ensure stable water conditions. To facilitate natural breeding behavior, each tank housed three males and three females, minimizing environmental stress. Fertilized embryos were collected 24 h after mating and incubated in egg buffer at 28 °C. Only healthy embryos at the early gastrulation stage (6 hpf) with intact chorionic membranes were selected for experimental use, while any unfertilized or non-viable embryos were excluded. Prior to experimental assays, fertilized embryos were examined under a dissecting microscope (Leica S6E with KL 300 LED, Schott, Germany) to ensure viability and developmental consistency [27].

Evaluation of XA3-Induced Acute Toxicity During Early Zebrafish Embryonic Development

OECD Test Guideline 236 (TG 236) was followed to assess the acute toxic effects of **XA3** on the early embryonic development in zebrafish. Embryos ($n = 10$) were placed in a 24-well plate with varying concentrations of **XA3** (0.7–12.5 µg/mL) and incubated at 28 °C. Mortality was recorded every 24 h up to 72 h to calculate the LD_{50}. The **XA3** test solution was changed daily to maintain solution freshness. For microscopic imaging, zebrafish embryos were dechorionated with forceps, anesthetized with tricaine (Sigma-Aldrich, St. Louis, MO, USA), and embedded in 3% methylcellulose at 24 hpf, 48 hpf and 72 hpf. Images were captured using a Leica DFC450C digital camera (Leica TL5000 Ergo transmitted light base) and processed with Leica Application Suite (Leica, Wetzlar, Germany) [27].

Evaluation of XA3 Effects on Blood Vessel Development, Cell Death and Apoptosis

To further investigate the effects of **XA3** on angiogenesis, transgenic zebrafish embryos (*Tg[kdrl: egfp]*) were treated with **XA3** at concentrations below the LD_{50} (0.7–3.125 µg/mL) at 10 hpf. A control group was treated with 0.1% DMSO, and vascular development was observed at 30 hpf for comparison. GFP fluorescence was qualitatively assessed as an indicator of blood vessel development and differentiation in response to the treatment. The treated embryos were then dechorionated and embedded in 3% methylcellulose on a glass slide for bioimaging, and live images were acquired using a CELENA® S Digital Imaging System (Logos Biosystems, Anyang, Korea). For more detailed analysis, the AO staining method was used to detect apoptotic cells in zebrafish embryos exposed to **XA3**. Live zebrafish larvae ($n = 5$) were immersed in 4 µg/mL AO solution (Sigma-Aldrich, St. Louis, MO, USA) for 20 min. The larvae were then rinsed with egg water several times for 5 min each, anesthetized with tricaine, and embedded in 3% methylcellulose. Live images were acquired using a CELENA® S Digital Imaging System (Logos Biosystems, Anyang, Korea) to analyse cell death [27].

In Vivo Evaluation of Anti-Melanogenic Properties of XA3 Using Zebrafish Embryo Model

Fertilised zebrafish embryos were collected 30 min post-fertilisation and initially treated with 200 µM PTU in egg water at 30 °C. Healthy embryos were selected for further experiments. At 24 hpf, the medium was replaced with fresh embryo water containing 1 µg/mL α-MSH together with either **XA3** (3.13–6.25 µg/mL) or kojic acid (7.10 µg/mL). Each treatment group contained more than 30 embryos. After a 24-hour exposure (up to 48 hpf), visual observations and digital images were acquired using the Leica Application Suite. Thirty (30) embryos were used to assess pigmentation, and another 30 embryos were used to assess tyrosinase activity.

For analysis of melanin content, embryos were homogenised in 500 µL lysis buffer (10 mM sodium phosphate, pH 6.8, 1% Triton X-100 and 1 mM PMSF) and then centrifuged. The resulting pellet was dissolved in 300 µL NaOH and incubated at 90 °C for 1 h before absorbance was measured at 405 nm. The supernatant lysate was used for the tyrosinase activity assay by adding L-DOPA and incubating at 37 °C for 30 min, followed by absorbance measurement at 450 nm. Melanin content and tyrosinase activity were calculated as described in the in vitro protocol [62, 63].

Statistical Analysis

All generated data were analysed with GraphPad Prism software (version 8, GraphPad Software Inc., La Jolla, CA, USA). Experiments were performed in triplicate, and results were independently analyzed for statistical significance using a one-way ANOVA, while an unpaired t-test was used for pairwise comparisons. Statistical significance was denoted as $*p < 0.05$, $**p < 0.005$, and $***p < 0.001$.

Supplementary Information The online version contains supplementary material available at https://doi.org/10.1007/s12247-026-10636-5.

Acknowledgements The authors expressed their gratitude to the Natural Medicine and Products Research Laboratory (NaturMeds), Universiti Putra Malaysia, as well as the Aquatic Animal Health Lab, College of Veterinary Medicine and the Research Institute of Veterinary Medicine, Chungnam National University, for their invaluable support. The resources and facilities provided by these laboratories significantly facilitated this research.

Author contributions **Amirah Hani Ramli** : Writing – original draft, Investigation, Formal analysis. **Puspanjali Swain** : Writing – original draft, Investigation, Formal analysis. **E. H. T. Thulshan Jayathilaka** : Writing – review & editing, Data curation, Validation. **Mawalle Kankanamge Hasitha Madhawa Dias** : Data curation, Validation. **Muhammad Syafiq Akmal Mohd Fahmi** : Data curation, Validation. **Emilia Abdul Malek** : Resources, Validation, Supervision. **Yaya Rukayadi** : Resources, Supervision. **Kok Wai Lam** : Resources, Supervision. **Yee Seng Tan** : Writing – review & editing, Data curation, Validation. **Chien Ing Yeo** : Writing – review & editing, Data curation, Validation. **Cheol-Hee Kim** : Writing – review & editing, Visualization, Resources, Conceptualization, Validation, Methodology, Supervision. **Mahanama de Zoysa** : Writing – review & editing, Visualization, Validation, Methodology, Data curation, Conceptualization, Methodology, Supervision. **Siti Munirah Mohd Faudzi** : Writing – review & editing, Visualization, Conceptualization, Methodology, Supervision, Project administration.

Funding Open access funding provided by The Ministry of Higher Education Malaysia and Universiti Putra Malaysia. This research was funded by Universiti Putra Malaysia, under the Geran Putra Berimpak (GPB/2022/9733100; with the vote number of 9733100) and the National Research Foundation of Korea (NRF) funded by the Korean government (MSIT) (2023R1A2C1006901, RS-2024-00443043).

Data Availability All data needed to evaluate the conclusions in the paper are present in the paper and/or the supplementary material. Additional data related to this paper may be requested from the authors.

Declarations

Ethical approval All zebrafish experiments were performed in compliance with the approved ethical policies and procedures of the Institutional Animal Care and Use Committee of Chungnam National University (approval number: 202404 A-CNU-077).

Competing interests The authors declare no competing interests.

References

1. Schwartz I, Smith S, Dingle T. Healthcare-associated infections and antimicrobial resistance: Something wicked this way comes: What health care providers need to know about *Candida auris*. Can Commun Dis Rep. 2018;44(11):271–6. 10.14745%2Fccdr.v44i11a01.
2. Lee SH, Park SY, Lee JS, Oh J. Infection of the Cavernous Sinus Caused by *Candida auris*. Korean J Healthcare-Associated Infect Control Prev. 2023;28(1):161–71. https://doi.org/10.14192/kjicp.2023.28.1.167.
3. Ghannoum M, Arendrup MC, Chaturvedi VP, Lockhart SR, McCormick TS, Chaturvedi S, Berkow EL, Juneja D, Tarai B, Azie N, Angulo D. Ibrexafungerp: a novel oral triterpenoid antifungal in development for the treatment of *Candida auris* infections. Antibiotics. 2020;9(9):539. https://doi.org/10.3390/antibiotics9090539.
4. Malik T, Mazhar E, Khan KH, Hussain S. Review article about superbug fungus C. auris. Preprints. 2021;20:2021060603. https://doi.org/10.20944/preprints202106.0603.v1.
5. Zhang Y, Guo D, Zhu Y, Liu I. Inhibition of mitochondrial function by approved drugs overcomes nasopharyngeal carcinoma chemoresistance. Anticancer Drugs. 2024;35(4):317–24. https://doi.org/10.1097/cad.0000000000001566.
6. Nett JE, Sanchez H, Cain MT, Andes DR. Genetic basis of *Candida* biofilm resistance due to drug-sequestering matrix glucan. J Infect Disease. 2010;202(1):171–5. https://doi.org/10.1086/651200.
7. Schinabeck MK, Long LA, Hossain MA, Chandra J, Mukherjee PK, Mohamed S, Ghannoum MA. Rabbit model of *Candida albicans* biofilm infection: liposomal amphotericin B antifungal lock therapy. Antimicrob Agents Chemother. 2004;48(5):1727–32. https://doi.org/10.1128/aac.48.5.1727-1732.2004.
8. Aliyu A. Effects of biofilm formation and plethora of *Candida* species causing ailments: a mini review. Gadau J Pure Allied Sci. 2022;1(2):200–10. https://doi.org/10.54117/gjpas.v1i2.27.
9. Araújo MGDF, Hilário F, Nogueira LG, Vilegas W, dos Santos LC, Bauab TM. Chemical constituents of the methanolic extract of leaves of Leiothrix spiralis Ruhland and their antimicrobial activity. Molecules. 2011;16(12):10479–90. https://doi.org/10.3390/molecules161210479.
10. Pinto E, Afonso D, Duarte S, Vale-Silva L, Costa E, Sousa E, Pinto M. Antifungal activity of xanthones: Evaluation of their effect on ergosterol biosynthesis by high-performance liquid chromatography. Chem Biol Drug Des. 2011;77(3):212–22. https://doi.org/10.1111/j.1747-0285.2010.01072.x.
11. Lin S, Sin WLW, Koh JJ, Lim F, Wang L, Cao D, Beuerman RW, Ren L, Liu S. Semisynthesis and biological evaluation of xanthone amphiphilics as selective, highly potent antifungal agents to combat fungal resistance. J Med Chem. 2017;60(24):10135–50. https://doi.org/10.1021/acs.jmedchem.7b01348.
12. Resende DI, Durães F, Zubarioglu S, Freitas-Silva J, Szemerédi N, Pinto M, Pinto E, Spengler P, Sousa G. Antibacterial potential of symmetrical twin-drug 3, 6-diaminoxanthones. Pharmaceuticals. 2024;17(2):209. https://doi.org/10.3390/ph17020209. Martins da Costa.
13. Wang J, Ding W, Wang R, Du Y, Liu H, Kong X, Li C. Identification and bioactivity of compounds from the mangrove endophytic fungus *Alternaria* sp. Mar Drugs. 2015;13(7):4492–504. https://doi.org/10.3390/md13074492.
14. Blanco-Ayala T, Lugo-Huitrón R, Serrano-López EM, Reyes-Chilpa R, Rangel-López E, Pineda B, Medina-Campos ON, Sánchez-Chapul L, Pinzón E, Cristina TS. Silva-Adaya, Antioxidant properties of xanthones from Calophyllum brasiliense: Prevention of oxidative damage induced by FeSO4. BMC Complement Altern Med. 2013;13:1–15. https://doi.org/10.1186/1472-6882-13-262.
15. Ruangsawasdi N, Boonnak N, Pruksaniyom C, Rodanant P. Xanthones Isolated from Cratoxylum cochinchinensis Reduced Oxidative Stress in Periodontal Ligament Stem Cells. Int J Mol Sci. 2023;24(19):14675. https://doi.org/10.3390/ijms241914675.
16. Naksuriya O, Okonogi S. Comparison and combination effects on antioxidant power of curcumin with gallic acid, ascorbic acid, and xanthone. Drug Discoveries Therapy. 2015;9(2):136–41. https://doi.org/10.5582/ddt.2015.01013.
17. Malekpoor M, Gharaghani S, Sharifzadeh A, Mirsattari SN, Massah A. Synthesis and antibacterial evaluation of novel xanthone sulfonamides. J Chem Res. 2015;39(8):433–7. https://doi.org/10.3184/174751915X14373971129805.
18. Singh O, Ali M, Akhtar N. New antifungal xanthones from the seeds of Rhus coriaria L. Z für Naturforschung C. 2011;66(1–2):17–23. https://doi.org/10.1515/znc-2011-1-203.
19. Kurniawan YS, Priyangga KT, Jumina,; Pranowo HD, Sholikhah EN, Zulkarnain AK, Fatimi HA, Julianus J. An update on the anticancer activity of xanthone derivatives: A review. Pharmaceuticals. 2021;14(11):1144. . https://doi.org/10.3390/ph14111144
20. Vanessa VV, Teh SS, Lam KW, Mah SH. Synthesis of 1-hydroxy-3-O-substituted xanthone derivatives and their structure-activity relationship on acetylcholinesterase inhibitory effect. Nat Prod Res. 2023;37(17):2849–61. https://doi.org/10.1080/14786419.2022.2137800.
21. Panda SS, Chand M, Sakhuja R, Jain SC. Xanthones as potential antioxidants. Curr Med Chem. 2013;20(36):4481–507.
22. Koh JJ, Zou H, Lin S, Lin H, Soh RT, Lim FH, Koh WL, Li J, Lakshminarayanan R, Verma C, Tan DT. Nonpeptidic amphiphilic xanthone derivatives: structure–activity relationship and membrane-targeting properties. J Med Chem. 2016;59(1):171–93. https://doi.org/10.1021/acs.jmedchem.5b01500.
23. Taylor S, Grimes P, Lim J, Im S, Lui H. Postinflammatory hyperpigmentation. J Cutan Med Surg. 2009;13(4):183–91. https://doi.org/10.2310/7750.2009.08077.
24. Park HJ, Lee YW, Choe YB, Ahn KJ. Skin characteristics in patients with pityriasis versicolor using non-invasive method, MPA5. Ann Dermatol. 2012;24(4):444–52. https://doi.org/10.5021/ad.2012.24.4.444.
25. Chang TS. Natural melanogenesis inhibitors acting through the downregulation of tyrosinase activity. Materials. 2012;5(9):1661–85. https://doi.org/10.3390/ma5091661.
26. Rosa GP, Palmiera A, Almeida IF, Kane-Pages A, Barreto MC, Sousa E, Pinto MM. Xanthones for melanogenesis inhibition: Molecular docking and QSAR studies to understand their anti-tyrosinase activity. Bioorg Med Chem. 2021;29:115873. https://doi.org/10.1016/j.bmc.2020.115873.
27. Ramli AH, Jayathilaka ET, Dias MK, Malek EA, Jain N, An J, Churchill DG, Rukayadi Y, Swain P, Kim CH, de Zoysa M, Mohd

Faudzi SM. Antifungal activity of synthetic xanthenone against fluconazole-resistant *Candida auris* and its mechanism of action. Microb Pathog. 2024;194:106797. https://doi.org/10.1016/j.micpath.2024.106797.

28. Abraham J, Jose B, Jose A, Thomas S. Characterization of green nanoparticles from plants. Phytonanotechnolog. 2020;21–39. https://doi.org/10.1016/B978-0-12-822348-2.00002-4.
29. Bakheit AH, Alkahtani HM. Integrated structural, functional, and ADMET analysis of 2-methoxy-4, 6-diphenylnicotinonitrile: the convergence of X-ray diffraction, molecular docking, dynamic simulations, and advanced computational insights. Molecules. 2023;28(19):6859. https://doi.org/10.3390/molecules28196859.
30. Ingham CJ, Schneeberger PM. Microcolony imaging of *Aspergillus fumigatus* treated with echinocandins reveals both fungistatic and fungicidal activities. PLoS ONE. 2012;7(4):e35478. https://doi.org/10.1371/journal.pone.0035478.
31. Bard GC, Taveira GB, Souza TA, Mello EO, Souza SB, Ramos AC, Carvalho AO, Pereira LS, Zottich U, Rodrigues R, Gomes VM. *Coffea canephora* peptides in combinatorial treatment with fluconazole: Antimicrobial activity against phytopathogenic fungus. Int J Microbiol. 2018;2018(1):8546470. https://doi.org/10.1155/2018/8546470.
32. Shao J, Shi G, Wang T, Wu D, Wang C. Antiproliferation of berberine in combination with fluconazole from the perspectives of reactive oxygen species, ergosterol and drug efflux in a fluconazole-resistant *Candida tropicalis* isolate. Front Microbiol. 2016;7:1516. https://doi.org/10.3389/fmicb.2016.01516.
33. Batoni G, Maisetta G, Esin S. Therapeutic potential of antimicrobial peptides in polymicrobial biofilm-associated infections. Int J Mol Sci. 2021;22(2):482. . https://doi.org/10.3390/ijms22020482.
34. Fox EP, Singh-Babak SD, Hartooni N, Nobile CJ. Biofilms and antifungal resistance, in Antifunugals: From genomics to resistance and the development of novel agents. Caister Academic; 2015.
35. Kowalski CH, Morelli KA, Schultz D, Nadell CD, Cramer RA. Fungal biofilm architecture produces hypoxic microenvironments that drive antifungal resistance. Proc Natl Acad Sci. 2020;117(36):22473–22483. https://doi.org/10.1073/pnas.2003700117
36. Shunmugaperumal T. Biofilm eradication and prevention: A pharmaceutical approach to medical device infections. Wiley; 2010.
37. Stewart P, Bjarnsholt T. Risk factors for chronic biofilm-related infection associated with implanted medical devices. Clin Microbiol Infect. 2020;26(8):1034–8. https://doi.org/10.1016/j.cmi.2020.02.027.
38. Hawas S, Verderosa AD, Totsika M. Combination therapies for biofilm inhibition and eradication: a comparative review of laboratory and preclinical studies. Front Cell Infect Microbiol. 2022;12:850030. https://doi.org/10.3389/fcimb.2022.850030.
39. Tits J, Cammue BP, Thevissen K. Combination therapy to treat fungal biofilm-based infections. Int J Mol Sci. 2020;21(22):8873. https://doi.org/10.3390/ijms21228873.
40. López-García J, Lehocký M, Humpolíček P, Sáha P. HaCaT keratinocytes response on antimicrobial atelocollagen substrates: Extent of cytotoxicity, cell viability and proliferation. J Funct Biomaterials. 2014;5(2):43–57. https://doi.org/10.3390/jfb5020043.
41. ISO 10993–5. Biological evaluation of medical devices—part 5: tests for *in vitro* cytotoxicity. Geneva: International Organization for Standardization; 2009.
42. Nagata T, Ito S, Itoga K, Kanazawa H, Masaki H. The mechanism of melanocytes-specific cytotoxicity induced by phenol compounds having a prooxidant effect, relating to the appearance of leukoderma. Biomed Res Int. 2015;20151:479798. https://doi.org/10.1155/2015/479798.
43. Oh MC, Fernando PD, Piao MJ, Kang KA, Iakmini Herath HM, Hyun JW. Baicalein inhibits α-melanocyte-stimulating hormone-stimulated melanogenesis via p38 mitogen-activated protein kinase pathway in B16F10 mouse melanoma cells. J Cancer Prev. 2023;28(2):40. https://doi.org/10.15430/JCP.2023.28.2.40.
44. Otang-Mbeng W, Sagbo IJ. Anti-melanogenesis, antioxidant and anti-tyrosinase activities of Scabiosa columbaria L. Processes. 2020;8(2):236. . https://doi.org/10.3390/pr8020236.
45. Masum MN, Yamauchi K, Mitsunaga T. Tyrosinase inhibitors from natural and synthetic sources as skin-lightening agents. Reviews Agricultural Sci. 2019;7:41–58. https://doi.org/10.7831/ras.7.41.
46. Chung KW, Jeong HO, Lee EK, Kim SJ, Chun P, Chung HY, Moon HR. Evaluation of antimelanogenic activity and mechanism of galangin in silico and in vivo. Biol Pharm Bull. 2018;41(1):73–9. https://doi.org/10.1248/bpb.b17-00597.
47. Lee Y, Song HY, Byun EB. Anti-melanogenic effects of hydroxyethyl chrysin through the inhibition of tyrosinase activity: *In vitro* and *in silico* approaches. Heliyon. 2025;11(2). https://doi.org/10.1016/j.heliyon.2025.e41718.
48. Singh K, Kashyap SK, Garg V. Use of zebrafish (Danio rerio) as a model for research in toxicological studies. J Appl Nat Sci. 2021;13(3):846. https://doi.org/10.31018/jans.v13i3.2767.
49. Ielciu I, Mouithys-Mickalad A, Franck T, Angenot L, Ledoux A, Păltinean R, Cieckiewicz E, Etienne D, Tits M, Crişan G, Frédérich M. Flavonoid composition, cellular antioxidant activity and (myelo) peroxidase inhibition of a *Bryonia alba* L. (Cucurbitaceae) leaves extract. J Pharm Pharmacol. 2019;71(2):230–9. https://doi.org/10.1111/jphp.13025.
50. Jurewicz A, Ilyas S, Uppal JK, Ivandic I, Korsching S, Mathur S. Evaluation of magnetite nanoparticle-based toxicity on embryo–larvae stages of zebrafish (*Danio rerio*). ACS Appl Nano Mater. 2020;3(2):1621–9. https://doi.org/10.1021/acsanm.9b02330.
51. Williams CH, Hong CC. Zebrafish small molecule screens: Taking the phenotypic plunge. Comput Struct Biotechnol J. 2016;14:350–6. https://doi.org/10.1016/j.csbj.2016.09.001.
52. Zhang C, Willett C, Fremgen T, Zebrafish. An animal model for toxicological studies. Curr Protoc Toxicol. 2003;17(1):1–7. https://doi.org/10.1002/0471140856.tx0107s17.
53. Qu J, Yan M, Fang Y, Zhao J, Xu T, Liu F, Zhang K, He L, Jin L, Sun D. Zebrafish in dermatology: a comprehensive review of their role in investigating abnormal skin pigmentation mechanisms. Front Physiol. 2023;14:1296046. https://doi.org/10.3389/fphys.2023.1296046.
54. Lajis AFB. A zebrafish embryo as an animal model for the treatment of hyperpigmentation in cosmetic dermatology medicine. Medicina. 2018;54(3):35. https://doi.org/10.3390/medicina54030035.
55. Gore AV, Monzo K, Cha YR, Pan W, Weinstein BM. Vascular development in the zebrafish. Cold Spring Harbor Perspective Med. 2012;2(5):a006684. https://doi.org/10.1101/cshperspect.a006684.
56. Zhang Y, Chen X, Gueydan C. J. Plasma membrane changes during programmed cell deaths. Cell Res. 2018;28(1):9–21. https://doi.org/10.1038/cr.2017.133. Han.
57. Karlsson J, Von Hofsten J, Olsson PE. Generating transparent zebrafish: a refined method to improve detection of gene expression during embryonic development. Mar Biotechnol. 2001;3:522–7. https://doi.org/10.1007/s1012601-0053-4.
58. Wusiman Z, Zhang AM, Zhang SS, Zhao PP, Kang YT, Zhang Y, Li ZJ, Huo SX. Galangin ameliorates PTU-induced vitiligo in zebrafish and B16F10 cells by increasing melanogenesis through activation of the p38/JNK MAPK pathway. Front Pharmacol. 2025;16:1521097. https://doi.org/10.3389/fphar.2025.1521097.
59. Rigaku O. CrysAlis PRO (Version 42), Diffraction, Yarnton, Oxfordshire, England, 2017.

60. Sheldrick GM. Crystal structure refinement with SHELXL. Cryst Struct Commun. 2015;71(1):3–8. https://doi.org/10.1107/S2053229614024218.
61. Farrugia LJ. WinGX and ORTEP for Windows: An update. Appl Crystallogr. 2012;45(4):849–54. https://doi.org/10.1107/S0021889812029111.
62. Ketata E, Elleuch H, Neifar A, Mihoubi W, Ayadi W, Marrakchi N, Rezgui F, Gargouri A. Anti-melanogenesis potential of a new series of Morita-Baylis-Hillman adducts in B16F10 melanoma cell line. Bioorg Chem. 2019;84:17–23. https://doi.org/10.1016/j.bioorg.2018.11.028.
63. Chen YM, Su WC, Li C, Shi Y, Chen QX, Zheng J, Tang DL, Chen SM. Anti-melanogenesis of novel kojic acid derivatives in B16F10 cells and zebrafish. Int J Biol Macromol. 2019;123:723–31. https://doi.org/10.1016/j.ijbiomac.2018.11.031.
64. Konuk HB, Ergüden B. Phenolic–OH group is crucial for the antifungal activity of terpenoids via disruption of cell membrane integrity. Folia Microbiol. 2020;65(4):775–83.
65. Rząd K, Ioannidi R, Marakos P, Pouli N, Olszewski M, Kostakis IK, Gabriel I. Xanthone synthetic derivatives with high anticandidal activity and positive mycostatic selectivity index values. Sci Rep. 2023;13(1):11893.
66. Banda-Flores IA, Torres-Tirado D, Mora-Montes HM, Peres-Flores G, Perez-Garcia LA. Resilience in resistance: The role of cell wall integrity in multidrug-resistant *Candida*. J Fungi. 2025;11(4):271.
67. Horton MV, Johnson CJ, Zarnowski R, Andes BD, Schoen TJ, Kernien JF, Lowman D, Kruppa MD, Ma Z, Williams DL, Huttenlocher A. Candida auris cell wall mannosylation contributes to neutrophil evasion through pathways divergent from Candida albicans and Candida glabrata. MSphere. 2021;6(3):00406–21. . https://doi.org/10.1128/msphere.
68. Vermitsky J-P, Edlind TD. Azole resistance in *Candida glabrata*: coordinate upregulation of multidrug transporters and evidence for a *Pdr1*-like transcription factor. Antimicrob Agents Chemother. 2004;48(10):3773–81.
69. Yi J, Zhang Q, Zhou H, Fei W, Liao J, Huang Y, Guo J. ROS-implicated apoptosis in *Candida albicans*: mechanistic insights into Aureobasidin A's antifungal activity. Front Microbiol. 2026;17:1725921.
70. Chimote G, Sreenivasan J, Pawar N, Subramanian J, Sivaramakrishnan H, Sharma S. Comparison of effects of anti-angiogenic agents in the zebrafish efficacy–toxicity model for translational anti-angiogenic drug discovery. Drug design, development and therapy, 2014: pp. 1107–1123.
71. Tal T, Kilty C, Smith A, LaLone C, Kennedy B, Tennat A, McCollum CW, Bondesson M, Knudsen T, Padilla S, Kleinstreuer N. Screening for angiogenic inhibitors in zebrafish to evaluate a predictive model for developmental vascular toxicity. Reprod Toxicol. 2017;70:70–81.
72. Hughes JP, Rees S, Kalindjian SB, Philpott KL. Principles of early drug discovery. Br J Pharmacol. 2011;162(6):1239–49.
73. Trevino-Rangel RDJ, Gonzalez GM, Montoya AMl, Rojas OC, Elizondo-Zertuche M. Alvarez-Villalobos, N.A. Recent antifungal pipeline developments against *Candida auris*: a systematic review. J Fungi. 2022;8(11):1144.
74. Lundvik H, Santini R, Altintop TU, Ozenci V, Andersson DI, Fatsis-Kavalopoulos N. Fast detection of synergy and antagonism in antifungal combinations used against *Candida albicans* clinical isolates. Sci Rep. 2025;15(1):36103.
75. Meletiadis J, Stergiopoulou T, O'Shaughnessy EM, Peter J, Walsh TJ. Concentration-dependent synergy and antagonism within a triple antifungal drug combination against Aspergillus species: analysis by a new response surface model. Antimicrob Agents Chemother. 2007;51(6):2053–64.